AIAA JOURNAL
Vol. 41, No. 4, April 2003

Plasma Study on Ionization of Flowing Gases by Direct Current Electric Discharge

Stelu Deaconu,* Hugh W. Coleman,† and S. T. Wu‡
University of Alabama in Huntsville, Huntsville, Alabama 35899

A new design of a corona/thermionic-arc discharge ionization device was investigated experimentally. The device features a hollow (spiral filament) cathode–plane anode configuration and creates a negative point to plane corona discharge, which ionizes a flowing gas column. Multiple experimental runs have been performed in nitrogen, helium, and argon. The diagnostics of the plasma consisted of electron temperature, electron density, gas pressure, and cathode/gas temperature. The measurements show that the discharge plasma and the plume are in local thermal nonequilibrium, with typical electron temperatures being one order of magnitude higher than the gas temperature. The experimental plasma data and the analysis of the experimental results are presented. The analysis focuses on the comparison of the experimental data with the charge-drift theory of the corona discharge and on identifying the stabilizing factors of the discharge. Finally, an approximate predictive model for the electron density in the plume is proposed.

Nomenclature

c	=	sound speed, $(\gamma RT)^{1/2}$
c_e	=	electron mean thermal speed, $(8k_bT_e/\pi m_e)^{1/2}$
c_p	=	heat capacity
$\vec{E}, \boldsymbol{E}$	=	vector electric field
e	=	electron charge
I	=	current
j	=	current density
k_b	=	Boltzmann's constant
M	=	Mach number, u/c
m_e	=	electron mass
m_i	=	ion mass
m_s	=	mass of gas particle
n_e	=	electron density
n_s	=	gas density
p	=	pressure
Q_{es}	=	electron collision cross section
R	=	gas constant
T, T_i	=	gas/ion temperature
T_e	=	electron temperature
u	=	gas speed
V	=	voltage
$\vec{v}, \boldsymbol{v}$	=	particle velocity
W	=	electric power
α	=	Townsend ionization coefficient
γ	=	gas specific heat ratio
ε_0	=	electrical permittivity of vacuum
λ_D	=	debye shielding length
μ_e, μ_i	=	electron/ion mobility
ν	=	collision frequency
ρ	=	charge density
ρ_1, ρ_2	=	gas density
ϕ	=	electric potential
χ	=	compression ratio
χ_M	=	thermionic emission coefficient

Received 23 August 2001; revision received 15 August 2002; accepted for publication 25 September 2002.

*Graduate Research Assistant, Department of Mechanical and Aerospace Engineering. Member AIAA.
†Eminent Scholar/Professor, Department of Mechanical and Aerospace Engineering. Associate Fellow AIAA.
‡Distinguished Professor, Department of Mechanical and Aerospace Engineering. Fellow AIAA.

Introduction

HYPERSONIC airbreathing propulsion systems with magnetohydrodynamic (MHD) bypass, for example, AJAX, are raising the problem of efficiently generating steady-state plasma flows with high ionization levels while minimizing the enthalpy addition to the flow. Theoretical investigations of electron beam[1] and nanosecond dc and rf pulse[2] ionization show that these methods are potential candidates for ionization of supersonic and hypersonic flows. However, electron beam ionization is disadvantaged by elaborate hardware requirements and the pulsed field ionization is in its incipient stages. An alternate ionization method proposed and investigated experimentally by the authors is the use of a dc-field corona/thermionic-arc discharge. In Ref. 3, the authors documented their initial findings and conclusions, and in Ref. 4 they presented a detailed description of the device and an efficiency study. This paper concentrates on the analysis of the data and the stability and theoretical modeling of the discharge. An approximate electron density model, scaled with the external electrical discharge parameters, is obtained.

For clarity, a brief description of the experimental setup is given here. The tests were carried out in a 0.75-m-long by 0.5-m-diam cylindrical glass vacuum chamber at pressures ranging from 200 to 700 mtorr. At its top, the vacuum chamber has an aluminum plate. Fitted through the top plate is a cylindrical microwave (MW) resonating chamber. The corona/thermionic discharge ionization device (CDID) was grafted onto the bottom of the MW resonating chamber (see Fig. 1a). The CDID has a radial–axial symmetry and consists of two electrodes. The aluminum end plate of the MW resonating chamber forms the anode of the ionization device. The cathode is made of a 0.8-mm tungsten–rhenium (95%W–5%Re) wire spiraled in the shape of a filament with an exterior diameter of 8 mm and having 20 turns. The cathode is 30 mm long and is mounted 40 mm below the anode plate on the axis of symmetry. An opening of 24 mm was machined in the center of the anode plate, and the upper side was fitted with a 75-mm-long, smooth stainless-steel pipe, as illustrated in Fig. 1b. The pipe is flared at the top and acts as a flow guide for the gas exiting the MW resonating chamber (which is used just as a gas reservoir). In this configuration, the modifications to the original MW system are minimal, and the CDID shares the gas feed system with the MW plasma generator.

The diagnostics of the discharge consist of measurements of 1) electrical parameters (voltage, current), 2) flow parameters (pressure, temperature), and 3) plasma electron density and electron temperature:

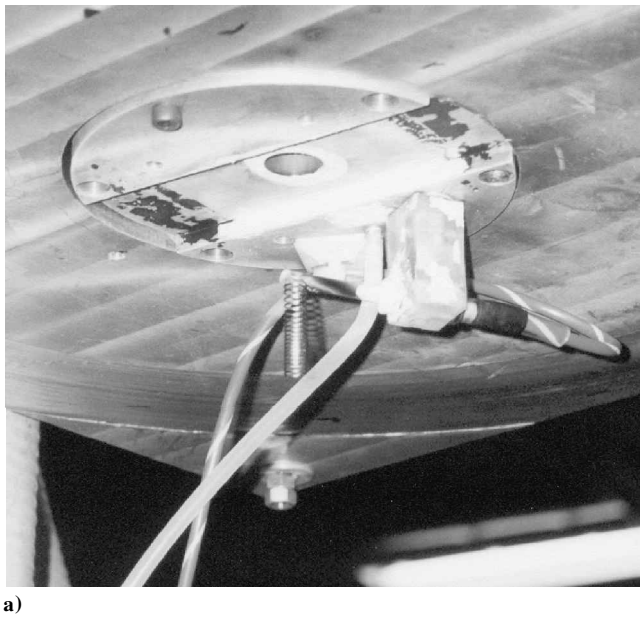

a)

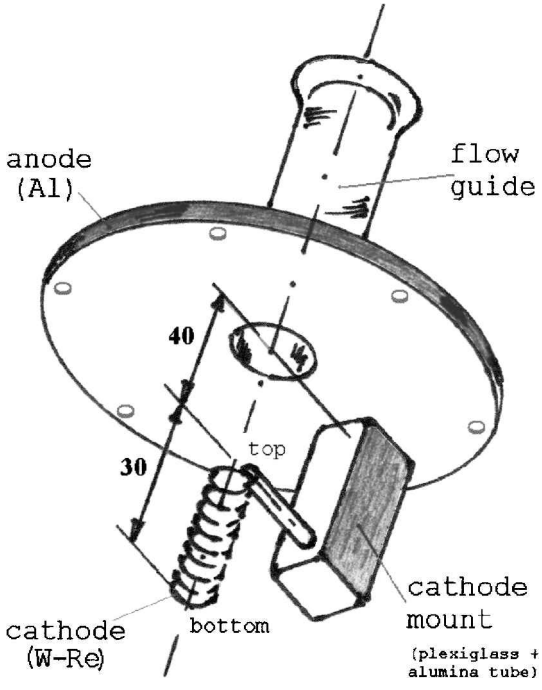

b)

Fig. 1 Corona discharge ionization device: a) photograph and b) diagram.

1) A high-voltage power supply drives the discharge in a voltage-controlled mode. The corona current is determined by the local plasma parameters through Ohm's law. Figure 2 illustrates the electrical circuit. The BC_1 power supply is an in-house designed, variable high-voltage rectifier capable of supplying a sustained power level of 1.5 kW. Two voltage-divider circuits (R_3–R_5 and R_4–R_6) are connected to the cathode line. They provide the cathode voltage and the current in the circuit. R_1 and R_2 are placed in series with the corona discharge, and they prevent the short circuiting of the power supply in case of discharge breakdown.

2) The pressures measured are the reservoir pressure p_1 (the MW resonating chamber) and the vacuum chamber pressure p_2. The gas and cathode temperature was measured by thermocouple and by infrared (IR) pyrometry.

3) Electron density and electron temperature radial distributions were obtained in a diametral plane of the plume, at a location approximately 30 mm below the cathode filament. These measurements were performed with a four-prong electric probe. For a more

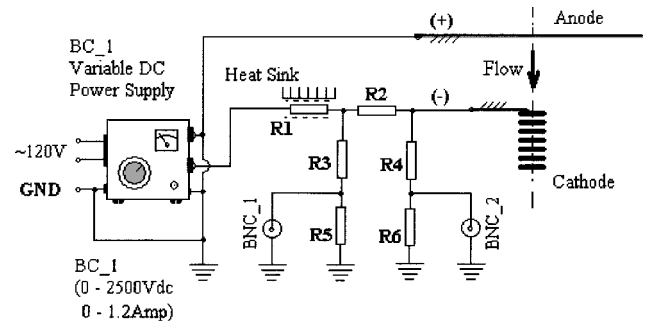

Fig. 2 CDID electrical circuit ($R_1 = 80\ \Omega/125$ W, $R_2 = 50\ \Omega/50$ W, $R_3 = R_4 = 8$ M $\Omega/5$ W, and $R_5 = R_6 = 5$ k $\Omega/1$ W); BNC_1 and BNC_2 are high-voltage probes.

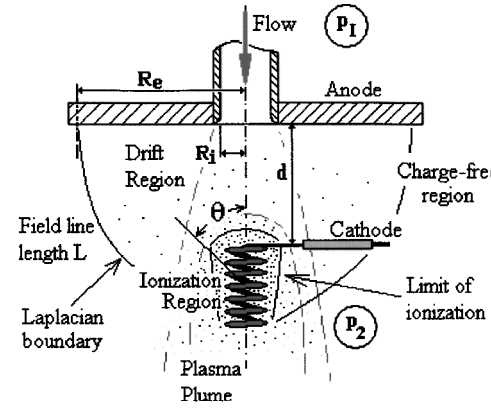

Fig. 3 CDID corona.

detailed description of the experimental procedures, the reader is referred to Ref. 4.

Corona Physics and CDID Ionization

Rigorously, the corona can be defined[5] as a self-sustained electrical gas discharge where the primary ionization processes take place in regions of high electric field. The two most common types of corona are the point-to-plane (rod-to-plane) and the concentric cylinder (wire–cylinder). In both of these geometries, one electrode has a much smaller area than the other and is the high-field or active electrode. The larger area electrode is the passive or low-field surface and usually acts as charge collector. Geometrically, the CDID corona belongs to the point-to-plane category with the cathode filament being the high-field electrode. The hollow cathode, the gas flow, and the thermionic emission of electrons at the cathode are the only notable departures from a typical corona discharge. From this standpoint, the CDID resembles a hollow cathode ion source[6] with the gas flowing in the opposite direction, that is, from the low-field to the high-field region.

Generally, a corona discharge can be divided into three interrelated regions. As illustrated in Fig. 3, the three regions are the ionization or active region, the drift region, and the charge-free region. Characteristic to the CDID corona is the existence of an additional fourth region, the plasma plume. The existence of these regions is dependent on the corona parameters: geometry, generating voltage, and gas properties. A typical CDID corona exhibits all of these regions, although the real extent of each can be estimated only approximately.

In the following section, the authors are aiming at an approximate theoretical treatment of the discharge. The goals of the analysis are to provide an explanation for the enhanced stability of the discharge and to obtain a relationship between the electron density in the plume and the electrical parameters of the discharge.

Starting at the boundary, the charge-free region is the interface of the discharge with its surroundings and is the simplest part of the corona. The only field variable of interest[7] is the Laplacian potential ϕ_0 from which the electric field $\boldsymbol{E}$ can be obtained. Inside

the Laplacian boundary is the drift region, which fills most of the anode–cathode space. The drift region is the defining characteristic of the corona discharge. The electrical equivalent of the drift region is a passive resistance placed in series with the discharge.[8] In this region, the electric potential is modified by space charge contributions $\phi = \phi_0 + \Sigma_i(\phi_i)$ and the charge carriers will drift along field lines with velocities proportional to their mobility $\boldsymbol{v} = \mu \cdot \boldsymbol{E}$. For the general case of a time-dependent discharge, the Poisson's equation $\nabla \bar{E} = \rho/\varepsilon_0$, $\boldsymbol{E} = -\nabla\phi$ can be combined with the charge continuity equation $\partial\rho/\partial t + \nabla(\bar{v} \cdot \rho) = 0$ to obtain the unipolar charge drift formula

$$\frac{\partial \rho}{\partial t} + \bar{v} \cdot \nabla\rho = -\rho\mu \cdot \nabla\bar{E} = -\frac{\mu\rho^2}{\varepsilon_0} \tag{1}$$

When Eq. (1) was derived, ion diffusion was neglected and the charge density $\Sigma_i n_i q_i$ was replaced by a unipolar ρ by considering charge carriers (here electrons) of one sign and constant mobility μ. Charge source terms are not present in the continuity equation, stemming from the assumption that an equilibrium is established between the production (impact by high-energy electrons) and the loss of charge (reattachment, recombination) in the drift region, that is, most free charges are neutralized at the electrodes. Equation (1) can also be written in terms of individual charge carriers if the aim is to reduce the error introduced by field averaging.[7,9] We assume for now that the unipolar treatment is fairly adequate for obtaining estimated charge mobility values in the drift region. A justification of this assumption will be given later in a subsequent section. During operation, the CDID reaches steady-state continuous glow and Eq. (1) becomes $\bar{v} \cdot \nabla\rho = -\rho\mu\nabla\bar{E} = -\mu\rho^2/\varepsilon_0$. Further transformation of Eq. (1) using $\nabla \cong 1/L$ and Poisson's equation gives $v \cdot \rho = \mu \cdot \varepsilon_0 E^2/L^2 = j_s$, which is the space charge current density. A more useful formula for the current density requires knowledge of the electric field distribution. Exact space charge saturated solutions for the electric field are summarized in Ref. 5. These are given in terms of the distance r from the ion source for plane geometry $E \sim r^{1/2}$ (Laplacian $E = \text{const}$) and cylindrical geometry $E = \text{const}$ (Laplacian $E \sim r^{-1}$), respectively. The field line geometry in the CDID corona starts out cylindrical and ends as a plane. Given the separation of the drift region from the cathode, a fair choice for the electric field is $E = \text{const} = V_0/L$, where V_0 is the applied external potential and L is the field line length. The space charge current density is, therefore,

$$j_s = v \cdot \rho = \mu\varepsilon_0\left(V_0^2/L^3\right) \tag{2}$$

If a hyperboloidal field geometry is assumed, the field lines are ellipses[8] of length $L = d[2\tan^2(\theta) + 1]^{1/2}$, with $\theta = \tan^{-1}(R/d)$. The current distribution within the drift region is given by the empirical Warburg distribution (see Refs. 5 and 8), $j(\theta) = j_0\cos^5(\theta)$, where $j_0 = \mu\varepsilon_0 V_0^2/d^3$, and all other parameters are shown in Fig. 3. When the experimentally observed span of the drift region $\theta \in (0, 60\text{ deg})$ is integrated over, the total current is obtained:

$$\begin{aligned} I &= 2\pi\int_0^{R_e} j_0\cos^5(\theta)\,\mathrm{d}r \\ &= 2\pi d^2 j_0 \int_{\theta_{\min}=0\text{ deg}}^{\theta_{\max}=60\text{ deg}} \cos^2(\theta)\cdot\sin(\theta)\,\mathrm{d}\theta \\ &\cong 2d^2 j_0 \end{aligned} \tag{3}$$

Finally, replacing j_0, the current is $I \cong 2\mu\varepsilon_0 V_0^2/d$, or

$$I/V_0 = 2 \cdot (\mu\varepsilon_0/d)V_0 \tag{4}$$

Both I and V_0 are measurable quantities in the external electrical circuit, and $d \cong 40$ mm. Equation (4) can be used to estimate the unipolar mobility of the charge carriers from the experimental data. However, it has been argued[5] that, because of the assumptions made, that is, linear potential and unipolar charge carriers, the use of Eq. (4) may (depending on experimental conditions) overestimate the actual mobility values. Thus, Eq. (4) will be employed mainly to show the coronalike behavior of the discharge, or the departure from this behavior, when the thermionic emission at the cathode becomes the predominant mechanism sustaining the discharge.

The physics of the ionization region are somewhat complicated because this is the volume where most of the energy transfer takes place. Only a short, qualitative description is given here. Ions drifting along the field lines that enter the sheath surrounding the cathode must have velocities greater than the Bohm velocity (see Ref. 10) $v_i \geq (k_b T_e/m_i)^{1/2}$. The discharge is a non-local-thermodynamic-equilibrium process with an electron temperature of about one order of magnitude higher than the ion (gas) temperature. As a result, a large amount of energy is transferred from ions to the cathode surface through collisions. There are two relevant consequences: 1) The cathode reaches temperatures that cannot be attained solely by ohmic heating. 2) Free electrons are produced by ion impact and thermionic emission at the cathode. The equilibrium thermionic current in the presence of an accelerating field is exponentially dependent on the cathode temperature[6,11,12] and is given by the Richardson–Dushman equation

$$j_{\text{th}} = A_M T^2 \cdot \exp\left(-\frac{\chi_M - 2ea \cdot E_w^{\frac{1}{2}}}{k_b T}\right) \tag{5}$$

where $a = 1.89 \times 10^{-5}\ (\text{V}\cdot\text{m})^{1/2}$ and E_w is the electric field at the cathode. The two coefficients A_M and χ_M are specific to the cathode material and can be found in literature. See, for instance, Refs. 11 and 13. For the tungsten filament we take $A_M = 70\ \text{A}/(\text{cm}^2\cdot\text{K}^2)$ and $\chi_M = 4.5$ eV. Additional ionization in this region is generated by electron avalanche (Townsend mechanism) due to impact by energetic primary (thermionic) electrons. Other processes taking place within the ionization region are reattachment, recombination, and the excitation of molecular vibrational modes and metastable states. The deexcitation of these metastable states results in the emission of quanta and is partially responsible for the bright appearance of the ionization region. The maximum electron density in the discharge is found in the ionization region and can be estimated from the condition[6] that the ion flux, $n_i \cdot v_i$ ($n_i = n_e$) across the cathode sheath must be equal to the flux of thermionic electrons emitted by the cathode, multiplied by the number of electrons, $\alpha \cdot l_e$ created in the ionization region $n_e \cdot v_i = \alpha \cdot l_e \cdot (j_{\text{th}}/e)$. The term in parenthesis is the flux of primary (thermionic) electrons in the cathode sheath, and l_e is some characteristic length of the ionization region. Recalling that the average ion velocity in the sheath is $(k_b T_e/m_i)^{1/2}$, the density of the plasma in the ionization region is

$$n_e \cong (m_i/k_b T_e)^{\frac{1}{2}} \cdot (\alpha \cdot l_e) \cdot (j_{\text{th}}/e) \tag{6}$$

Clearly, Eq. (6) is derived by assuming that the electric field is high enough to maintain an ionization coefficient greater than the attachment coefficient. Also note that the charge density in the ionization region is exponentially dependent on the cathode temperature through j_{th}. Therefore, Eq. (6) is, at best, an average estimate of the overall electron density in the ionization region.

Finally, the plume is the region of interest for the experimenters and is formed by the flowing gas, which sweeps the ionized particles downstream of the ionization region. The field intensity in the plume is minimal and little additional energy is added to the plasma. Thus, the ionization fraction in the plume is determined mainly by the recombination rate.

The second important aspect of the CDID operation is the gas flow. The solution to the corona flow is obtained from the basic conservation laws, mass, momentum, and energy, written such that the only unknowns are the experimentally measured parameters. For simplicity, consider the plume quasi one dimensional. Written with the standard notation between two successive states, the one-dimensional mass, momentum, and energy conservation equations[14] for flow with heat addition are

$$\begin{aligned} \rho_1 u_1 = \rho_2 u_2, \qquad p_1 + \rho_1 u_1^2 = p_2 + \rho_2 u_2^2 \\ c_p T_1 + u_1^2/2 + q = c_p T_2 + u_2^2/2 \end{aligned} \tag{7}$$

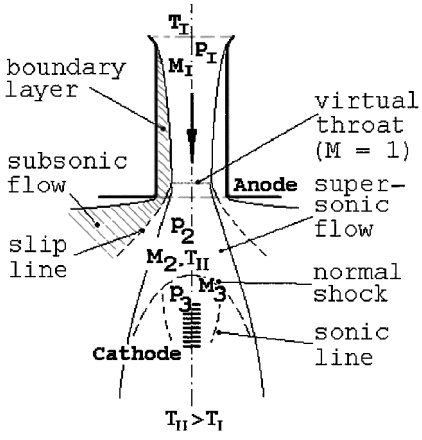

Fig. 4 CDID flow pattern.

where q is the added heat per unit mass, p_I is the total (stagnation) upstream pressure, and T_I is the total upstream temperature. Additionally, we can write the ideal equation of state, $p = \rho RT$, and the isentropic pressure and adiabatic temperature relations

$$p_I = p_1\left\{1 + [(\gamma - 1)/2]M_1^2\right\}^{\gamma/(\gamma-1)}$$

$$T_I = T_1\left\{1 + [(\gamma - 1)/2]M_1^2\right\} \tag{8}$$

Heat addition to the flow is the primary effect of the discharge. A secondary effect of the ionization process is the decrease[15] of the effective adiabatic coefficient γ of the gas. A noticeable γ change in the CDID flow can only be expected in regions with a significant ionization fraction (i.e., the immediate neighborhood of the cathode), and, thus, γ is assumed constant throughout the flow.

In a quasi-one-dimensional isentropic flow approximation, the velocity of the jet at the reservoir exit is a function of the p_2/p_I pressure ratio. The experimental pressure data indicate that argon and nitrogen reach sonic speed in the flow guide, whereas helium flow remains subsonic. The two situations corresponding to the downstream flow are 1) supersonic expansion, normal shock at cathode (Ar, N_2) and 2) subsonic recompression (He). The supersonic solution is the case of interest and is discussed further.

Even with the simplifying assumptions, an exact one-dimensional shock solution of Eq. (7) is difficult to obtain. The difficulty stems from 1) the inability to model the shock–heat interaction properly with only the available data and 2) the downstream flow not being adiabatic. Specifically, the stagnation pressure and temperature ahead of the shock, as well as the aft shock pressure, cannot be estimated, and, thus, the location of the shock cannot be anchored. To circumvent this difficulty, we disregard the shock and assume that the heat is added to the entire downstream region (Fig. 4). Solving Eqs. (7) and (8) for upstream (flow-guide) and downstream (interelectrode space) Mach numbers, one obtains

$$\frac{M_1^2\left\{1 + [(\gamma - 1)/2]M_2^2\right\}}{M_2^2\left\{1 + [(\gamma - 1)/2]M_1^2\right\}^{(\gamma+1)/(\gamma-1)}} = \frac{(p_2/p_I)^2}{T_{II}/T_I}$$

$$\frac{1 + \gamma \cdot M_1^2}{1 + \gamma \cdot M_2^2} \cdot \frac{1}{\left\{1 + [(\gamma - 1)/2]M_1^2\right\}^{\gamma/(\gamma-1)}} = \frac{p_2}{p_I} \tag{9}$$

When Eq. (9) was obtained, the temperature downstream, T_2, was approximated using the adiabatic stagnation temperature T_{II}, although the adiabatic condition is violated. In doing this, it is assumed that the error introduced is acceptable for this approximate one-dimensional model. Also note that a shock solution of Eq. (7) with $p_{II} = p_I$ and $T_{II} = T_I$ and $p_3 = \chi \cdot p_2$ and $T_{III} = T_I + q/c_p$ (i.e., heat addition only aft shock) is not mathematically possible for any compression ratio $\chi > 1$. This substantiates the assumption that heat is actually added in the entire downstream region and, therefore, justifies the use of Eq. (9). The solution of Eqs. (9) yields the flow Mach number ahead of the shock, M_2 and, consequently, the shock strength.

Experimental Results

There were 19 successful experimental runs performed. The test names are given by the attempted test pressure p_2 in the vacuum chamber, and the test matrix is given in Table 1.

The CDID testing was performed in two phases: 1) plasma flow and electric property measurements and 2) pyrometric temperature measurements with similar test conditions. To increase the lifetime of the cathode, the power levels in these tests were kept below 1 kW. The relevant test results for argon and nitrogen are displayed in Table 2. W_0 is the total power supplied to the CDID, and T is the average gas temperature in the ionization region. We note that the actual pressure in the vacuum chamber does not exactly match the test name pressure (see Table 2, column 2).

Plasma parameters are characteristic to the plume region downstream of the cathode. Characteristic to both the argon and the nitrogen plumes is the exponential decay of the electron density with radius. Results from a typical probe scan are presented in Fig. 5. Electron temperature profiles in these tests show little radial change, which suggests rapid thermalization of the electrons leaving the ionization region.

The nitrogen coronas exhibited good stability, as is illustrated by the data in Fig. 5, which show little scattering. A more significant amount of scatter was observed in the argon density profiles, and it was attributed to the occasional spark breakdown in the discharge gap during the four-prong probe scan.

In terms of electron density, helium yielded the poorest results. Densities measured are in the mid-10^{15} m^{-3} range, and the average electron temperature is 4–4.5 eV. This situation was due to constant onset of breakdown instabilities. Although the helium plasma is of little practical use, the helium tests provided insight into the stabilization mechanism of the CDID discharge.

A large portion of the experimental data consists of cathode and gas temperature measurements. In the CDID the cathode is the main source of ion heating, whereas heating by electron collision is only secondary or marginal. Cathode radiation/convection is responsible for dissipating more than 60% of the total power input. Generally, the cathode heating is nonuniform due to field concentration and convection cooling (Fig. 6).

Table 1 CDID test matrix

Test pressure, mtorr	No. of tests		
	Ar	He	N_2
200	N/A	N/A	1
300	2	2	2
400	2	N/A	2
500	N/A	1	3
600	N/A	1	3

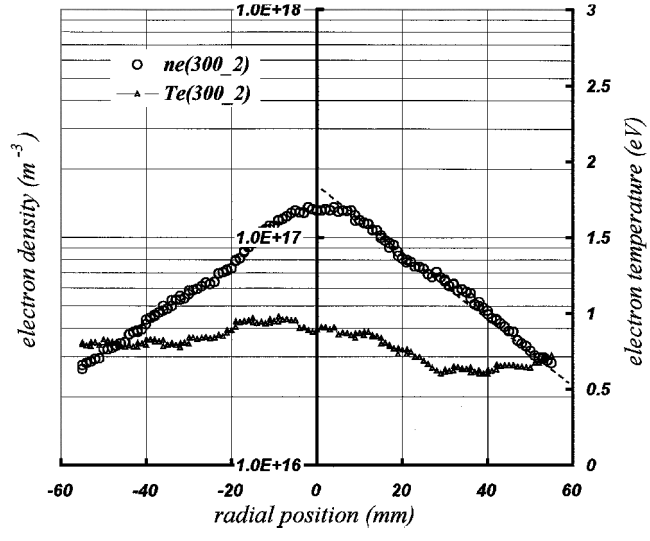

Fig. 5 Electron density and temperature (test N_2, 300_2, radial probe scan 30 mm below the cathode).

Table 2 Argon and nitrogen data

Test	p_2, mtorr	p_1, mtorr	V_0, V	I, A	W_0, W	$n_e \times 10^{-17}$ average, m^{-3}	$n_e \times 10^{-18}$ maximum, m^{-3}	T, K	T_e, eV
					Argon				
300_1	247	668	857	0.65	530	2.4	1.0	604	0.39
300_2	255	670	888	1.07	906	8.1	2.1	773	0.31
400_1	355	1360	657	0.78	493	4.2	2.0	673	0.27
400_2	350	1350	634	1.03	600	7.0	2.9	763	0.23
					Nitrogen				
200_1	200	406	1489	0.557	830	0.45	0.10	873	1.04
300_1	274	639	1369	0.560	768	0.30	0.08	860	1.00
300_2	237	609	1337	0.663	887	0.52	0.13	961	0.80
400_1	368	887	1239	0.710	884	0.25	0.10	1016	1.08
400_2	376	929	1183	0.719	850	0.44	0.12	1009	1.09
500_2	515	1214	1032	0.808	834	0.80	0.20	811	0.74
500_3	575	1192	1057	0.556	589	0.47	0.14	800	0.89
500_5	602	1105	1097	0.760	834	0.86	0.24	827	1.28
600_2	699	1519	959	0.813	777	0.88	0.25	895	0.73
600_3	699	1519	952	0.776	739	0.86	0.24	884	0.69
600_4	692	1526	950	0.774	736	0.83	0.26	883	0.70

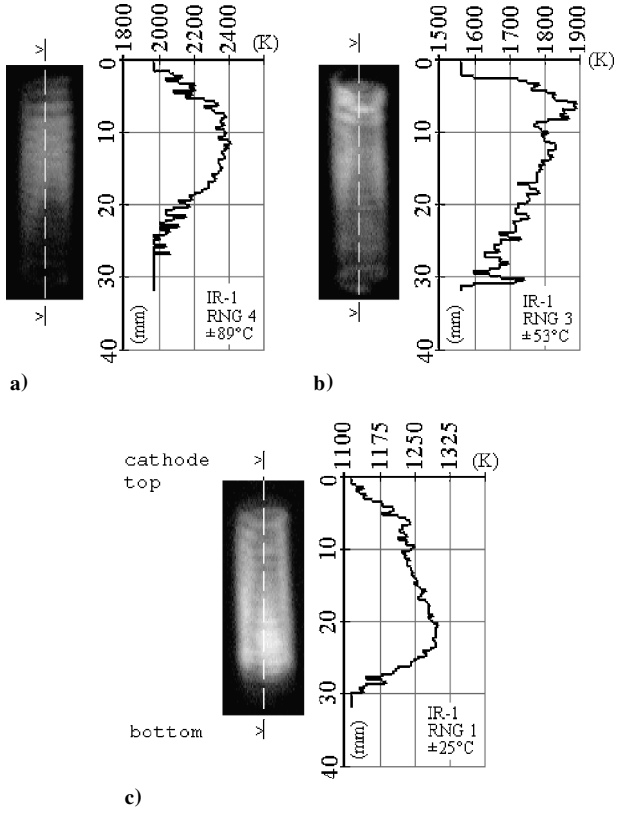

Fig. 6 Convection effects on cathode temperature: a) nitrogen, b) argon, and c) helium (IR cathode imaging).

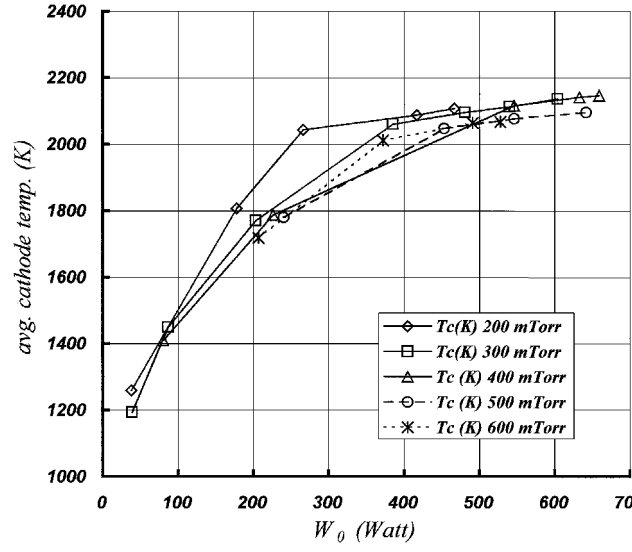

Fig. 7 Average cathode temperature (N_2 tests, from average pixel intensity of IR cathode images).

The IR camera shows regions of the filament being heated to temperatures 10–15% higher than the average. The cooling patterns in Fig. 6 are consistent with the convective properties of the three gases used. In argon ($c_p = 0.51$ kJ/kgK) the cathode exhibits a hot spot near the top (Fig. 6b), whereas in helium ($c_p = 5.2$ kJ/kgK) the cathode is cooled most at the top (Fig. 6c). Figure 7 illustrates the overall effect of convection and radiation on the average cathode temperature.

Two regions are distinguishable in Fig. 7, a convection region for power levels lower than 300 W and a saturation region above 400 W where the radiation loss is significant. The higher temperature gradient in the low-power region is a direct consequence of an inadequate dissipation mechanism (radiation is less effective). An increased cooling effect due to convection is evident in the high-pressure tests.

The exact distribution of the thermionic current density along the cathode is inferred from the spatially resolved cathode temperature profile. Figure 8a presents the graph of the cathode temperature profile in a 500 mtorr/642 W nitrogen temperature test (not included in Table 2), obtained by plotting the IR image of the cathode as a flat (two-dimensional) surface.

The current density is given by Eq. (5). The electric field at the cathode is $E_w \cong \phi_w/\lambda_D$, where the cathode fall is given by[16] $\phi_w \cong (k_b T_e/2e) \cdot \ln(\pi \cdot m_e/8 \cdot m_i) = 12.6$ V. Figure 8b shows the calculated thermionic current density. The average thermionic current is 433 A/m^2 when summed over the entire cathode surface. The difference from the current density measured in the external circuit, $j_{\exp} = 505$ A/m^2, is about 15%. Clearly, for this test, thermionic emission is the main mechanism of sustaining the discharge current at the cathode.

Discussion

The emphasis in this section is placed on the nitrogen data because they are the most complete. The unipolar mobility of the charge carriers can be estimated from the experimental data using Eq. (4). Figure 9 presents a combined I/V_0 vs V_0 plot of all nitrogen tests. The linear variation of the data implies that the corona current–voltage relation is rather insensitive to changes in gas pressure.

The slope of the data is proportional to the average mobility of the charge carriers. The negative sign of the slope confirms that the current is preponderantly sustained by negative charges. With the data in Table 2, the estimated carrier, that is, electron, mobility [from Eq. (4)] in the nitrogen discharge is 560 m^2/V · s for the low-current

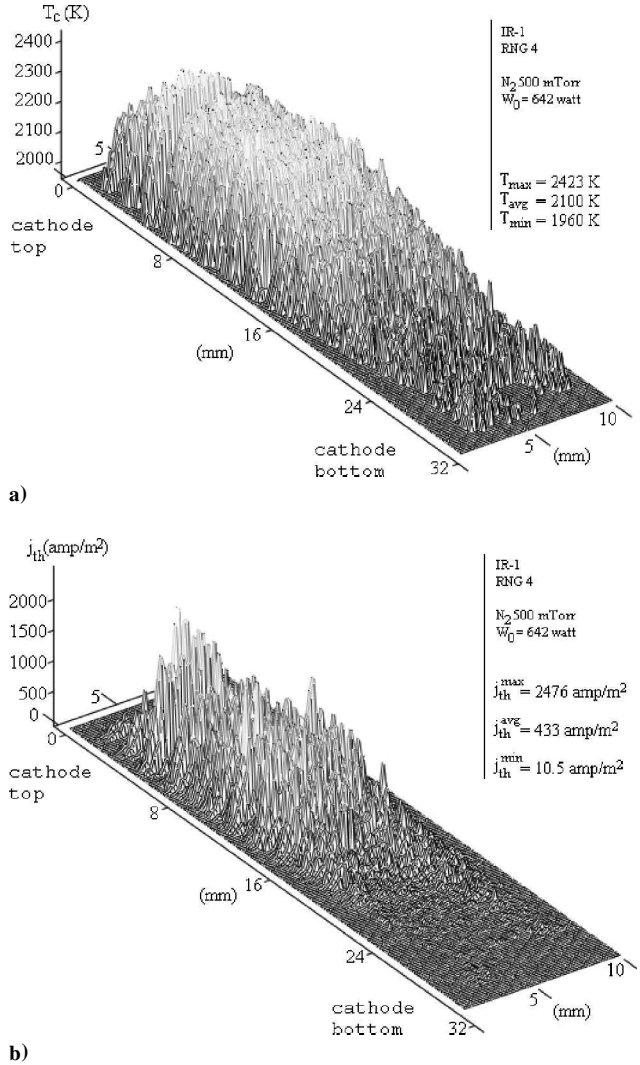

Fig. 8 Two-dimensional view of the cathode surface: a) temperature and b) current distribution (N_2, 500 mtorr, and $W_0 = 642$ watt, from IR cathode images).

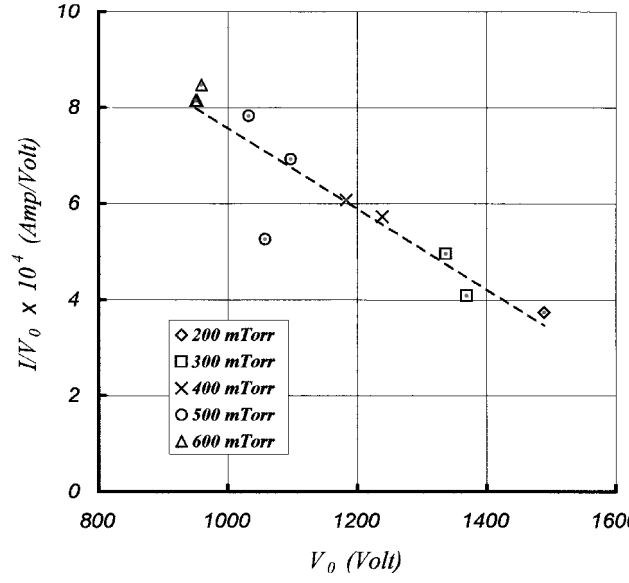

Fig. 9 Corona current–voltage plot (N_2 tests).

tests and 1900 $m^2/V \cdot s$ for the high-current tests. For argon, Eq. (4) yields average electron mobilities of 2000–4800 $m^2/V \cdot s$. These values agree well with mobility estimates from collision cross section data only for small currents.[4] As the discharge current increases, Eq. (4) overestimates the true mobility values in the discharge, as predicted by Sigmond and Goldman.[5] The explanation for this behavior is that at high currents, the discharge changes from corona (ionization in regions of high field) to thermionic arc (current maintained mainly by thermionic emission at the cathode).

We note that, close to the axis, the flowfield is aligned with the electric field and has a net effect of increasing the current due to the positive ions. This effect is implicitly lost in the unipolar charge drift formulation. Let us now justify the unipolar drift assumption by estimating the magnitude of the ion current density. The ion current density is proportional to ion velocity $\mu_i \cdot E + v$. The mobility of ions is $\mu_i = e/m_i \cdot \nu_{is}$, where ν_{is} is the collision frequency of ions with neutrals. For instance, the average test conditions in the drift region of the nitrogen corona ($p_2 = 300$–500 mtorr, $T = 400$–500 K, and $E = 200$ V/cm) give the ion collision frequency $\nu_{is} \cong 10$ GHz and the mobility $\mu_i = 3 \times 10^{-4}$ $m^2/V \cdot s$. The ion velocity due to field acceleration is $\mu_i \cdot E \cong 6.8$ m/s. The flow in the nitrogen tests is slightly supersonic and, therefore, $v \cong c = (\gamma RT)^{1/2} = 400$ m/s. Thus, the effect of the flow is a large increase of the ion current, or, equivalently, a two-order-of-magnitude effective increase of the ion mobility to 0.02 $m^2/V \cdot s$. By comparison, the electron mobility is five orders of magnitude higher, and, thus, the ion current contribution can be neglected.

The flow plays a more significant role in the discharge as a stabilizing factor. The stabilizing mechanism is two sided, so that 1) the shock recompresses the gas in the ionization region and 2) the flow removes heat and charge from the ionization region. These two flow effects are discussed further.

The stabilizing effect of the shock recompression lies with the operating values of the field-to-gas density ratio E/n_s. In general, the discharge tends to destabilize in regions of high E/n_s. The shock recompression reduces the local value of this ratio by increasing the gas density. To exemplify the recompression effect numerically, we choose test 400_2 [$p_I = 929$ mtorr (123.5 Pa), $p_2 = 376$ mtorr (50 Pa), $T_I = 300$ K, and $T_{II} = 1009$ K]. Solving Eq. (9), we obtain $M_1 = 0.21$ in the flow guide and $M_2 = 1.05$ ahead of the shock. The aft shock static pressure is $p_3 \cong 1.12 \cdot p_2$, whereas, at the cathode, the pressure is increased to the stagnation value $p_{III} \cong 2 \cdot p_2$. The density of the gas in the ionization region reaches stagnation values $\rho_{III} \cong 1.65\rho_2$. The density increase is sufficient to compensate the increase in the E/n_s ratio due to field concentration at the cathode. In effect, the shock is a stabilizing boundary. This mechanism suggests that a higher-Mach-number flow would be a more efficient stabilizing factor due to a higher degree of aft shock recompression. It also explains the unstable behavior of the helium corona. The helium flow is subsonic and the gas density in the ionization region is low. Consequently, the E/n_s ratio is high and the discharge collapses frequently.

A local increase in gas temperature triggers a destabilizing energy exchange feedback loop between the discharge and the flow called thermal instability.[13] The second flow stabilization mechanism is the convective heat removal from the ionization region (Fig. 6). Generally, the flow cools the region of high electric field at the top of the cathode, inhibiting the onset of thermal instabilities. A secondary stabilizing effect of the cooling process is a local reduction of the cathode thermionic emission. The number of primary electrons emitted into the ionization region is reduced, and, thus, the local energy density is lowered. As a result, the feedback temperature increase loop is removed, and the discharge is stabilized. Argon has the poorest cooling properties, and the cathode forms a hot spot at the top (Fig. 6b), whereas the nitrogen realizes a more uniform cooling along the cathode length. Figure 6a shows that, in nitrogen, the maximum cathode temperature does not coincide with the region of highest field strength at the cathode top. This stabilizing effect of the flow explains the better stability of the nitrogen over the argon discharge.

The instabilities developed in the three gases are dissimilar, as is illustrated in Fig. 10. Helium instabilities are explosive, symmetric, and involve a large volume of the drift region (Fig. 10a). Nitrogen instabilities show asymmetry (Fig. 10c) and are also caused by gap breakdown in the drift region, whereas in argon, the discharge

a)

b)

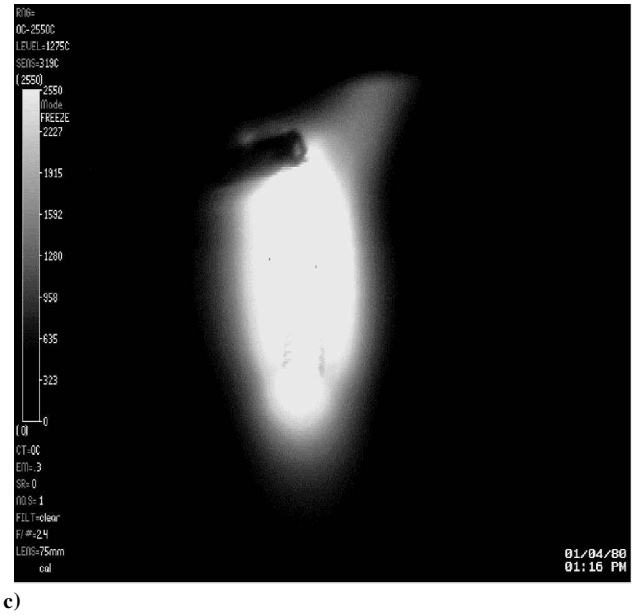

c)

Fig. 10 CDID corona instabilities: a) helium, b) argon, and c) nitrogen.

breakdown is at random to the lower vacuum chamber walls (Fig. 10b). The exact breakdown mechanism is unknown. The patterns of light recorded by the camera suggest the development of anode-directed streamer channels.[13] A probable breakdown mechanism in argon is the development of streamer channels triggered by runaway electrons, which are accelerated along field lines parallel to the cathode surface.

The electron density distribution along the cathode is similar to the thermionic current distribution profile (see Fig. 8b), and its maximum [Eq. (6)] is attained in the ionization region. The ionization coefficient α for various gases and E/p conditions is tabulated in Ref. 13. With the average CDID test conditions, the ionization coefficients are $\alpha \cong 0.7\ \text{cm}^{-1}$ for nitrogen and $\alpha \cong 1.1\ \text{cm}^{-1}$ for argon. If it is assumed that the characteristic length of the ionization region of the order of electron mean free path $1/n_s \cdot Q_{es} \cong 1$ cm, the maximum electron density is in the mid-10^{18} m^{-3} range in nitrogen and low-10^{19} m^{-3} range in argon.

It is more useful to predict plasma density in the plume based on electrical parameters measured in the discharge circuit. An exact relationship between the electron density in the plume and power, current, or applied voltage is difficult to find on theoretical grounds due to discharge complexity. Instead, the authors have attempted to derive a simple approximation starting from Eq. (6). Rewriting the current density in terms of electron mobility, we have

$$\begin{aligned} n_e &= (m_i/k_b T_e)^{\frac{1}{2}} \cdot [(\alpha \cdot I)/(e \cdot A_c)] \cdot (1/n_s Q_{es}) \\ &= (m_i/k_b T_e)^{\frac{1}{2}} \cdot \left[(\alpha \cdot I)\Big/\left(e^2 \cdot A_c\right)\right] \cdot \mu_e m_e c_e \end{aligned} \tag{10}$$

where A_c is the cathode emission surface area. When Eq. (4) and $c_e = (8k_b T_e/\pi \cdot m_e)^{1/2}$ are used, the electron density in the ionization region becomes

$$n_e = [(8/\pi) m_i m_e]^{\frac{1}{2}} \cdot \left[(\alpha \cdot d)\Big/\left(1.55 \cdot \varepsilon_0 e^2 A_c\right)\right] \cdot (I/V_0)^2 \tag{11}$$

The electron density in the plume is dependent mainly on the recombination rate. Recombination describes the process of electron density decay in time and can only affect the magnitude of the density profile downstream but not its shape. Some distortion of the electron density profile can be expected due to the radial expansion of the plume as it travels downstream. Accordingly, we estimate that the maximum electron density in the plume (i.e., the peak of the electron density curve in Fig. 5) follows an approximate profile given by

$$n_e \sim (I/V_0)^2 \tag{12}$$

The $n_{e(\max)}$ data in Table 2 scaled with Eq. (12) produce the following results:

$$n_e \times 10^{-18} = 0.09 \cdot (I/V_0)^2 \times 10^7 + 0.634 \tag{13}$$

for argon and

$$n_e \times 10^{-18} = 0.03 \cdot (I/V_0)^2 \times 10^7 + 0.042 \tag{14}$$

for nitrogen, where n_e is per cubic meter and $(I/V_0)^2$ is in ampere per volt squared. Graphically, the electron density vs $(I/V_0)^2$ is depicted in Fig. 11.

The different slopes of the nitrogen and argon electron densities, when scaled with $(I/V_0)^2$, are easily explained when it is noted [see Eq. (11)] that the electron density is proportional to the $\alpha \cdot m_i^{1/2}$. With average values of the ionization coefficient of 0.7 cm^{-1} for nitrogen and 1.1 cm^{-1} for argon, and $m_i(\text{Ar})/m_i(\text{N}_2) = 1.43$, Eq. (11) predicts that the slope of n_e in argon must be twice as large as in nitrogen. Experimentally, the $n_e(\text{Ar})/n_e(\text{N}_2) \cong 3$. The difference can be explained by the different cathode heating patterns over the emitting area A_c in the two gases. Equations (13) and (14) can be used to estimate electron densities in the plume of the discharge by measuring only two external electrical parameters, voltage and current.

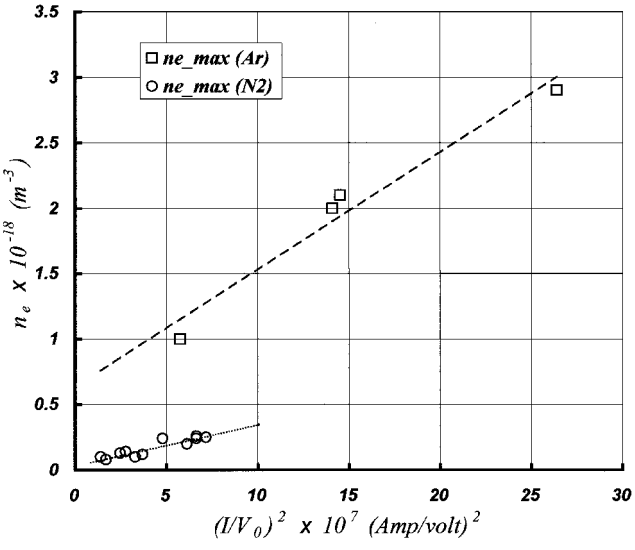

Fig. 11 Electron density scaling in the plume.

Conclusions

Experiments with a dc corona discharge ionization device have shown that steady electron densities of 10^{17}–10^{18} part/m^3 can be obtained in nitrogen and argon flows. These ionization levels are in the range necessary for efficient MHD energy extraction from ionized supersonic flows. It was shown that, in a supersonic flow, the normal shock in front of the cathode is an effective stabilizing boundary for the electric discharge. The stabilization mechanism suggests that higher-Mach-number flows would increase the stabilizing effect. A plume electron density model based on the electrical parameters of the discharge was obtained.

Acknowledgments

This research program was sponsored in part by the NASA Marshall Space Flight Center and by the Air Force Office of Scientific Research under Contract F 49620-98-0-0083. The authors thank Paul Vaughan for his assistance in setting up the experimental apparatus and Brian Landrum for his insightful comments during the preparation of the manuscript.

References

[1]Macheret, S. O., Shneider, M. N., and Miles, R. B., "Electron-Beam-Generated Plasmas in Hypersonic Magnetohydrodynamic Channels," *AIAA Journal*, Vol. 39, No. 6, 2001, pp. 1127–1138.

[2]Macheret, S. O., Shneider, M. N., and Miles, R. B., "Modeling of Plasma Generation in Repetitive Ultra-Short DC, Microwave, and Laser Pulses," AIAA Paper 2001-2940, June 2001.

[3]Deaconu, S., Coleman, H. W., and Wu, S. T., "Experimental Study of the Ionization of Flowing Gases by DC Corona Discharge," AIAA Paper 2001-2943, June 2001.

[4]Deaconu, S., Coleman, H. W., and Wu, S. T., "Experimental Characterization of a Thermionic-Arc Discharge Ionization Device for Flowing Gases," *Review of Scientific Instruments*, Vol. 73, No. 1, 2002, pp. 91–97.

[5]Sigmond, R. S., and Goldman, M., "Corona Discharge Physics and Applications," *NATO Advanced Science Institute Series B, Physics*, Vol. 89B, 1981, pp. 1–65.

[6]Ferreira, C. M., and Delcroix, J. L., "Theory of the Hollow Cathode Arc," *Journal of Applied Physics*, Vol. 49, No. 4, 1978, pp. 2380–2395.

[7]Jones, J. E., "On the Global Variational Principles for Corona Discharges with Particular Reference to the Active Glow Region," *Journal of Physics D: Applied Physics*, Vol. 33, 2000, pp. 389–395.

[8]Sigmond, R. S., "Simple Approximate Treatment of Unipolar Space-Charge-Dominated Coronas: The Warburg Law and the Saturation Current," *Journal of Applied Physics*, Vol. 53 No. 2, 1982, pp. 891–898.

[9]Jones, J. E., "On Analytic Solutions of the Drift Equations for Many Ionic Species," *Journal of Physics D: Applied Physics*, Vol. 27, 1994, pp. 1835–1847.

[10]Chen, F. F., *Introduction to Plasma Physics and Controlled Fusion, Volume I: Plasma Physics*, 2nd ed., Plenum, New York, 1984, p. 293.

[11]Sutton, G. W., and Sherman, A., *Engineering Magnetohydrodynamics*, McGraw–Hill, New York, 1965, Chap. 6.

[12]Melissinos, A. C., *Experiments in Modern Physics*, Academic Press, New York, 1966, pp. 65–70.

[13]Raizer, Y. P., *Gas Discharge Physics*, Springer-Verlag, Berlin, 1991.

[14]Anderson, J. D., *Fundamentals of Aerodynamics*, McGraw–Hill, New York, 1984, Chap. 8.

[15]Zel'dovich, Y. B., and Raizer, Y. P., *Physics of Shock Waves and High Temperature Hydrodynamic Phenomena*, edited by W. D. Hayes and R. F. Probstein, Vol. 1, Academic Press, New York, 1966, Chap. 3.

[16]Vriens, L., Smeets, A. H. M., and Cornelissen, H. J., "Modeling of a Glow Discharge," *NATO Advanced Science Institute Series B, Physics*, Vol. 89B, 1981, pp. 65–117.

M. Sichel
Associate Editor